AGU PUBLICATIONS

Geophysical Research Letters

RESEARCH LETTER
10.1002/2015GL064770

Key Points:
- First instrumentally recorded tsunamis in the New Britain trench
- Slow rupture velocities estimated from seismic and tsunami analyses
- Different tsunamis in earthquake doublet due to different location and depth

Supporting Information:
- Figures S1–S9

Correspondence to:
M. Heidarzadeh,
mheidar@eri.u-tokyo.ac.jp

Citation:
Heidarzadeh, M., A. R. Gusman, T. Harada, and K. Satake (2015), Tsunamis from the 29 March and 5 May 2015 Papua New Guinea earthquake doublet (M_w 7.5) and tsunamigenic potential of the New Britain trench, *Geophys. Res. Lett.*, *42*, 5958–5965, doi:10.1002/2015GL064770.

Received 31 MAY 2015
Accepted 6 JUL 2015
Accepted article online 14 JUL 2015
Published online 30 JUL 2015

Tsunamis from the 29 March and 5 May 2015 Papua New Guinea earthquake doublet (M_w 7.5) and tsunamigenic potential of the New Britain trench

Mohammad Heidarzadeh[1], Aditya Riadi Gusman[1], Tomoya Harada[1], and Kenji Satake[1]

[1]Earthquake Research Institute, University of Tokyo, Tokyo, Japan

Abstract We characterized tsunamis from the 29 March and 5 May 2015 Kokopo, Papua New Guinea, M_w 7.5 earthquake doublet. Teleseismic body wave inversions using various rupture velocities (V_r) showed similar source-time functions and waveform agreements, but the spatial distributions of the slips were different. The rupture durations were ~45 and ~55 s for the March and May events, with their peaks at ~25 and at ~17 s, respectively. Tsunami simulations favored source models with V_r = 1.75 and 1.50 km/s for the March and May earthquakes. The largest slip on the fault was similar (2.1 and 1.7 m), but the different depths and locations yielded maximum seafloor uplift of ~0.4 and ~0.2 m. Tsunami simulation from hypothetical great earthquakes (M 8.4 and 8.5) on the New Britain trench showed that tsunami amplitudes may reach up to 10 m in Rabaul, but most tsunami energy was confined within the Solomon Sea.

1. Introduction

An earthquake doublet with moment magnitude (M_w) 7.5 occurred in Kokopo, Papua New Guinea, on 29 March and 5 May 2015. According to the United States Geological Survey (USGS), the earthquake origin times, the epicenters, and depths were 23:48:31 Greenwich mean time on 29 March at 4.763°S 152.561°E and 41 km for the first event, and 01:44:05 on 5 May at 5.465°S 151.886°E and 42 km for the second event (Figure 1). These two earthquakes, which occurred in the New Britain subduction zone, caused no damage and fatalities. According to local authorities, both earthquakes were followed by tsunamis. The height of the first tsunami was around half a meter in the nearby city of Rabaul whereas some tsunami oscillations were reported in the Rabaul harbor due to the second event. Following these earthquakes, tsunami threat forecasts were issued by the Pacific Tsunami Warning Center which were cleared a few hours later for both cases.

The epicentral areas are part of the Pacific Ring of Fire and are among the world's most complicated areas in terms of tectonic setting. The region is home to several minor and major plates such as the Indo-Australian, Solomon Sea, North and South Bismark Seas, Woodlark and Pacific plates forming several subduction zones, and submarine ridges (Figure 1). The 29 March and 5 May 2015 earthquakes occurred in the New Britain subduction zone where the Solomon Sea plate is subducting beneath the South Bismark Sea Plate to the northwest and beneath the Pacific Plate to the northeast (Figure 1). The region is seismically active and experienced 22 earthquakes with magnitudes equal or larger than 7.5 since A.D. 1900 among which the largest events were two M 8.1 earthquakes in 1971 and 2007 (Figure 1) [*United States Geological Survey*, 2015; *Lay and Kanamori*, 1980; *Chen et al*., 2009]. Several earthquake doublets were previously reported by *Lay and Kanamori* [1980] in this region.

Although the tsunamigenic potential of the adjacent areas such as the Solomon Islands and Papua New Guinea was studied by some authors [e.g., *Chen et al*., 2009; *Fritz and Kalligeris*, 2008; *McAdoo et al*., 2008; *Synolakis et al*., 2002; *Tappin et al*., 2001; *Heidarzadeh and Satake*, 2015], this area remains among world's least studied regions in terms of tsunami hazards. Specifically, possible tsunami hazard from the New Britain subduction zone has not been studied before. Although the 29 March and 5 May 2015 Papua New Guinea (PNG) earthquakes were of moderate size, the resulting tsunamis were the first instrumentally recorded tsunamis in the New Britain trench and, hence, are of importance for regional tsunami hazard assessment. Here we contribute to assessment of the tsunami hazards of the New Britain subduction zone by studying these two tsunamis. We study available tide gauge and Deep-ocean Assessment and Reporting of Tsunamis (DART) records, perform teleseismic body wave inversion and

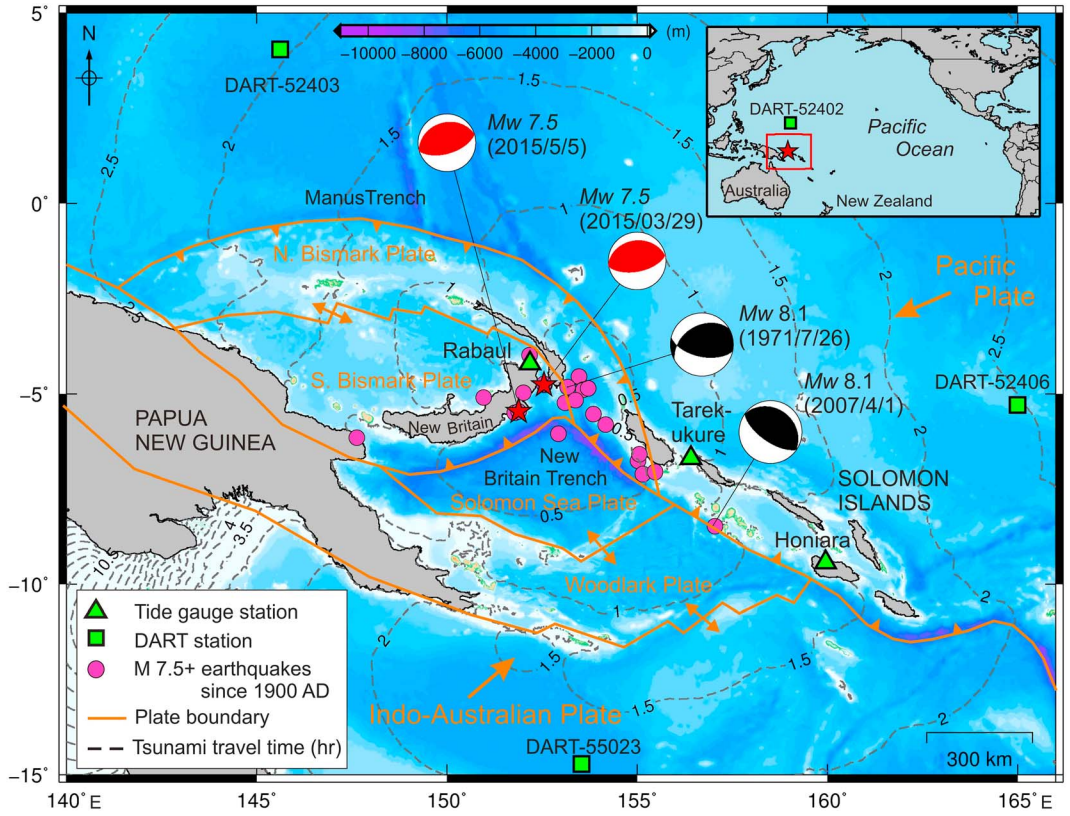

Figure 1. Epicentral areas and tectonic setting. Bathymetry of the region and epicenters of $M > 7.5$ earthquakes since 1900 A. D. (filled pink circles) from USGS earthquake catalog. Focal mechanisms of the 2007; March and May 2015 earthquakes are from USGS, while that of the 1971 is from *Lay and Kanamori* [1980]. The magnitude of the 1971 earthquake was reported as M_S 7.9 by *Lay and Kanamori* [1980]. Plate motion arrows are approximated. Plate boundaries are based on *Yoneshima et al.* [2005] and *Pegler et al.* [1995]. Dashed lines show tsunami traveltimes in hours from the tsunami of 29 March 2015.

numerical modeling of tsunami propagation to characterize the earthquakes and tsunamis, and propose the rupture models of the earthquake doublet. We then study regional tsunami hazards from hypothetical great earthquakes.

2. Data and Methodology

Accurate estimation of earthquake rupture velocity is of importance for earthquake source studies because it is an important dynamic parameter of faulting process. *Satake* [1987] showed that seismic inversion is stable temporally, while tsunami inversion is stable spatially, because seismic wave velocity is higher than typical rupture velocity, while tsunami velocity is much lower. *Lay et al.* [2014] observed strong trade-offs between spatial slip distribution and the assumed rupture velocity for teleseismic body wave inversions and proposed to jointly use seismic and tsunami data. *Gusman et al.* [2015] showed that results of teleseismic body wave inversions alone cannot appropriately constrain the source area of the 1 April 2014 Iquique (Chile) earthquake and applied tsunami observations to do so. Therefore, in this study, we combine teleseismic body wave inversion and tsunami simulation and waveform analysis.

The fault parameters for teleseismic body wave inversion were based on global centroid moment tensor solutions (http://www.globalcmt.org/CMTsearch.html) as strike: 259° and dip: 25° for the March event and strike: 247° and dip: 37° for the May event. The slip amount and rake angles for each subfault were derived from our teleseismic body wave inversion, which was performed applying *Kikuchi and Kanamori*'s [1991] method using 63 and 56 *P* wave vertical components, for the March and May earthquakes, respectively, recorded at distances between 30° and 100° from the epicenter (see Figures S1 and S2 in the supporting information for station locations). The data were provided by the Incorporated Research Institutions for Seismology Data Management Center (IRIS DMC). The waveforms were band-pass filtered for the

frequency between 0.004 and 1.0 Hz. A maximum rupture duration of 7.5 s was considered for each subfault consisting of four overlapping isosceles triangles with a duration of 3 s separated by 1.5 s intervals. Rupture velocity (V_r) was varied from 1.0 to 2.75 km/s with 0.25 km/s intervals resulting in eight different solutions for each earthquake. The velocity structure around the source region was set in reference to the CRUST 2.0 [*Bassin et al*., 2000] and ak135 [*Kennett et al*., 1995].

The tsunami records at two tide gauge stations, Tarekukure Wharf and Honiara, and at four DART stations were provided by the Intergovernmental Oceanographic Commission and U.S. National Oceanic and Atmospheric Administration (NOAA), respectively (see Figure 1 for locations and Figures 2c and 2d for the tsunami records). The sampling interval was 1 min. The nearby tide gauge station of Rabaul was out of order at the time of the earthquakes (I. Itikarai, personal communications, 2015). High-pass filter of Butterworth Infinite Impulse Response digital filters [*Mathworks*, 2015] with a cutoff frequency of 0.00027 Hz was used for removing tidal signals from the original records. The fast Fourier transform (FFT) was used for spectral analysis of tsunami waveforms for which we applied the FFT function in MATLAB program [*Mathworks*, 2015].

Tsunami propagation was numerically simulated using computer model of *Satake* [1995], which solves shallow water equations using a finite difference method on a staggered grid system. A time step of 1.0 s was used for tsunami simulations. Bathymetry data were provided by the 30 arc sec GEBCO-2014 bathymetric grid [*Intergovernmental Oceanographic Commission et al*., 2003]. In our simulations, inundation of tsunami on dry land was not included. A vertical wall boundary on the shoreline was assumed. Hence, application of the 30 arc sec bathymetry grid was accurate enough to carry out the simulations. Instantaneous coseismic seafloor deformation was used as the tsunami source calculated using analytical formula by *Okada* [1985]. Tsunami travel time (TTT) analysis was performed using the TTT program provided by *Geoware* [2011].

3. Results

Results of teleseismic body wave inversions showed that the moment-rate, or source-time, functions estimated using rupture velocities from 1.0 to 2.75 km/s were very similar. The agreements between the observed and simulated waveforms, in terms of root-mean-square (RMS) misfits, were also similar (see Figures S3 and S4 for examples of source-time functions and the waveform fits for different rupture velocities). However, the spatial distributions of slip were significantly different (Figures S5 and S6). For the May event, the slip distribution from $V_r = 1.0$ km/s was overlooked because it was very different from other seven slip distributions. For the March earthquake, the major slip region of the solution using $V_r = 1.0$ km/s was located ~20 km south of the epicenter, whereas that using $V_r = 2.75$ km/s was located ~70 km southeast of the epicenter (Figure S5). We were unable to select the best one out of the various source models for each earthquake.

The 29 March tsunami was clearly recorded at Tarekukure tide gauge station and three DART stations of 55023, 52403, and 52406 (Figure 2c; black waveforms). Maximum trough-to-crest amplitude was 8.4 cm in Tarekukure and was 1–2 cm at the DART stations (Figure 2). Spectral analysis showed that tsunami source period band was 10–20 min (Figure S7). We could not detect tsunami signal at Honiara, meaning that it must be in the range of the background noise (~1 cm) at this station. The 5 May tsunami was smaller than the March one and was clear only at DART 55023 with a wave height of ~0.6 cm and a period of ~10 min (Figure 2d; black waveform).

For both events, we conducted tsunami simulations using all slip distributions obtained from our teleseismic body wave inversions and then compared the simulated waveforms with the observed ones. Unlike teleseismic body wave inversions in which waveform fits were almost similar for all source models, the computed tsunami waveforms were different from one source model to another (Figures S8 and S9). For the March tsunami, the simulated wave from model $V_r = 2.5$ km/s was arriving ~4 min earlier, and its period was shorter than the observed one (Figure S8g). We compared the first wave of simulations with that of the observations because first tsunami wave is usually representative of the tsunami source and later waves may be mixed with other effects. The RMS misfit between the observations and simulations were calculated in order to select the best source model (Figures 2e and 2f). For the March tsunami, the smallest

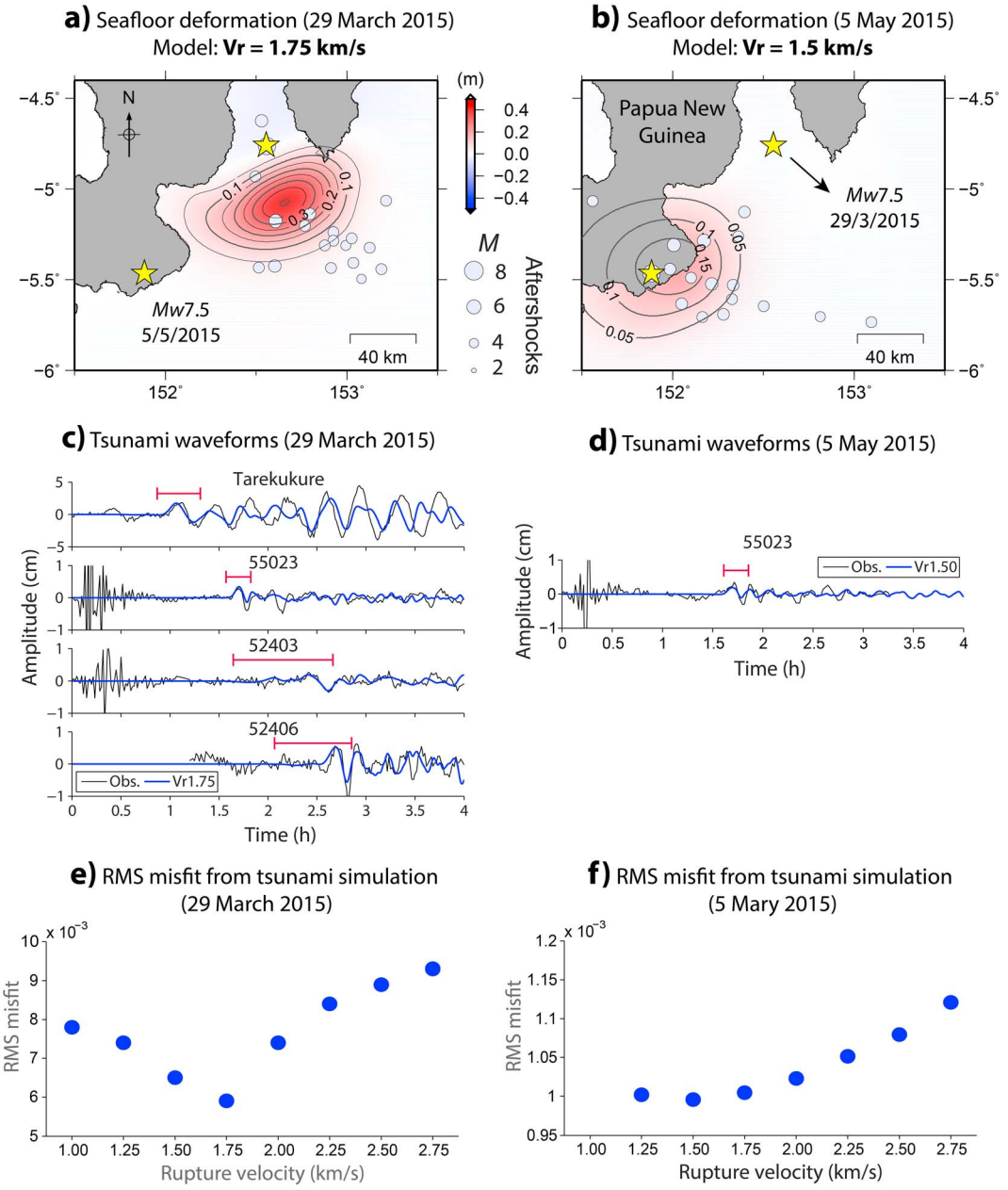

Figure 2. (a) Seafloor deformation due to the slip distribution resulted from $V_r = 1.75$ km/s for the 29 March 2015 PNG earthquake. Gray circles show 1 day aftershocks. The seafloor deformation contours begin from 0.05 m with 0.05 m intervals. (b) The same as Figure 2a but from the source model $V_r = 1.50$ km/s for the 5 May 2015 PNG earthquake. (c) Comparison of the observed (black) and simulated (blue) tsunami waveforms at one tide gauge and three DART stations for the source model from $V_r = 1.75$ km/s for the 29 March 2015 PNG earthquake. The red horizontal bars indicate parts of the waveforms that were used for RMS misfit calculations. (d) Comparison of the observed (black) and simulated (blue) tsunami waveform at DART 55023 for the source model from $V_r = 1.50$ km/s for the 5 May 2015 PNG earthquake. (e, f) RMS misfits for observed and simulated tsunami waveforms for all source models for the 29 March and 5 May 2015 PNG earthquakes.

RMS misfit was obtained for $V_r = 1.75$ km/s (Figures 2c and 2e). Here by decreasing the rupture velocity from 2.5 to 1.75 km/s, the slip moves toward the epicenter, in shallower water. As a result, the distance between observational stations and the major slip region increases (except for DART 52403); hence, the traveltimes of the simulated tsunami become similar to the observed ones. In addition, the computed waveforms are different because the decrease in water depth at the tsunami source results in an increase in tsunami period. For the May tsunami, the best fit was obtained using the source model with $V_r = 1.50$ km/s

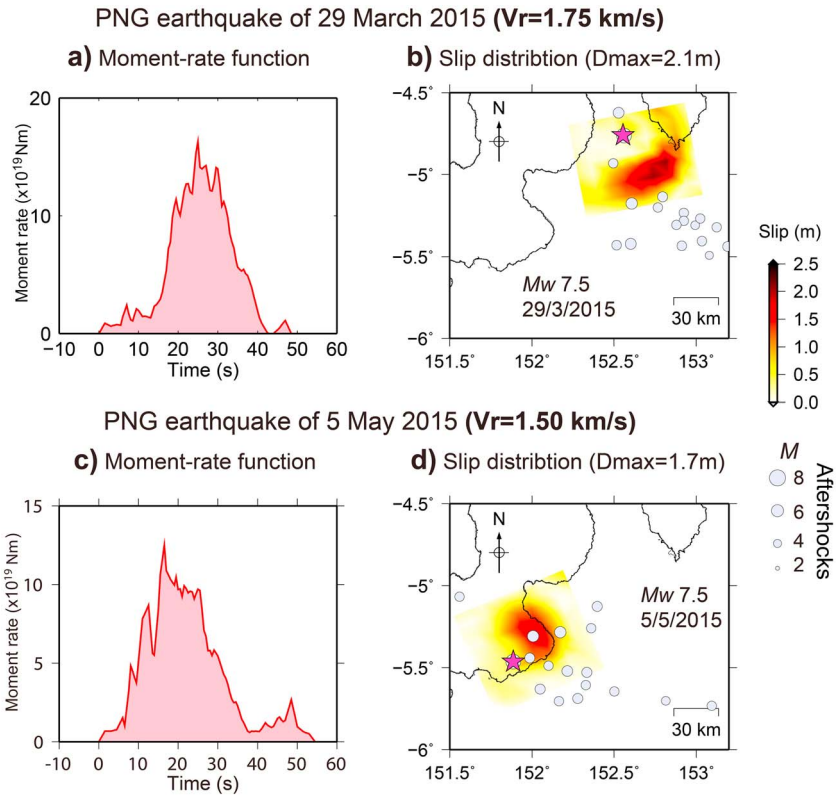

Figure 3. Moment-rate functions and slip distributions of our final source models for the 29 March and 5 May 2015 PNG earthquakes. Gray circles show 1 day aftershocks. D_{max} represents maximum slip amount.

(Figures 2d, 2f, and S9), although the RMS for the single station does not vary as much as the March event. Seafloor deformations due to best source models of the two earthquakes are shown in Figures 2a and 2b, indicating that the maximum uplift due to the March event was around twice larger than that from the May one.

In summary, for the March earthquake, the source model from the rupture velocity of 1.75 km/s was consistent with the results of teleseismic body wave inversion and tsunami simulations. The seafloor deformation, with uplift larger than 5 cm of our final source model, had an area of 110 km × 60 km, with a center located ~35 km south of the epicenter (Figure 2a). The seismic moment of this source model was 2.15×10^{20} N m equivalent to the moment magnitude of 7.5. The estimated moment-rate function implied total rupture duration of ~45 s with its peak energy at ~25 s (Figures 3a and 3b). For the May event, the best model was from $V_r = 1.50$ km/s (Figures 3c and 3d). The seafloor deformation, with uplift larger than 5 cm of our final source model, had an area of 100 km × 80 km, with a center located ~15 km east of the epicenter beneath the New Britain Island (Figure 2b). The seismic moment of this source model was 1.89×10^{20} N m equivalent to the moment magnitude of 7.45. Total rupture duration was ~55 s with its peak energy at ~17 s (Figure 3c). The second event had a slightly smaller seismic moment and earlier peak energy compared to the first event.

4. Discussion

Although the 5 May 2015 PNG earthquake was of the same magnitude of the 29 March one, the resulting tsunami from the May earthquake was not as large as the March one. The reasons were as follows: (1) the largest slip (2.1 m) of the March event was located at shallower depth than the largest slip (1.7 m) of the May event; hence, the maximum seafloor uplift was ~0.4 m for the March event (Figure 2a), whereas that from the May event was ~0.2 m (Figure 2b); and (2) parts of the seafloor deformation due to the May earthquake were located inland (Figure 2b).

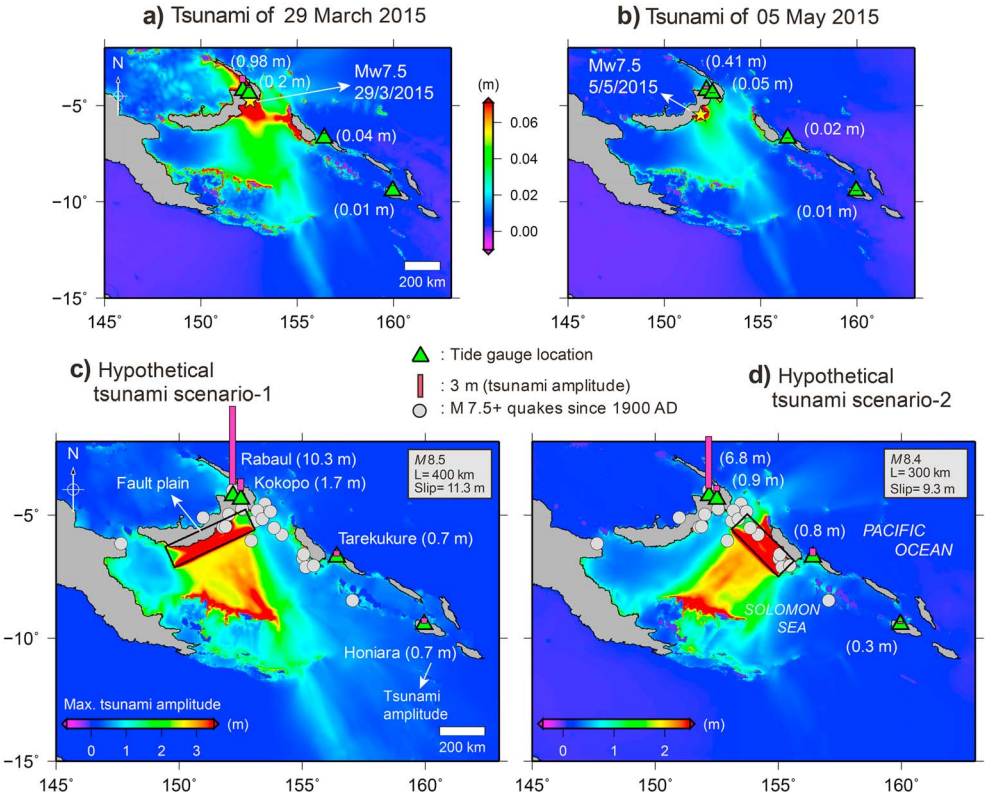

Figure 4. (a, b) Distribution of maximum simulated tsunami amplitudes resulted from the 29 March and 5 May 2015 events. Numbers in parentheses indicate maximum observed tide gauge tsunami amplitudes except for Rabaul which is from simulations. (c, d) Distribution of maximum simulated tsunami amplitudes resulted from two large tsunami scenarios. The tsunami amplitudes here are shoreline tide gauge zero-to-crest amplitude. Runup heights can be larger than these values.

The recent large tsunamis following the giant interplate earthquakes offshore Japan and Indonesia demonstrated that earthquakes larger than our anticipation may occur in any subduction zone [*Satake*, 2014; *Lay*, 2012; *McCaffrey*, 2007; *Satake and Atwater*, 2007; *Stein and Okal*, 2007]. While the largest recorded earthquake in the Solomon Sea region is *M* 8.1, it may not represent the largest possible event because of the short time span of the available earthquake instrumental records. As clues to understand tsunami hazards from the New Britain subduction zone, we modeled two scenario tsunamis resulting from hypothetical *M* 8.5 and *M* 8.4 earthquakes representing the full rupture of its west and east flanks, respectively (Figures 4c and 4d). Empirical relationships can be used to relate earthquake magnitudes with fault dimensions and average slips for hypothetical earthquake scenarios [e.g., *Murotani et al*., 2013; *Wells and Coppersmith*, 1994]. Using empirical relationships by *Wells and Coppersmith* [1994] and by assuming a fixed fault width of 80 km and two fault lengths of 300 and 400 km, the moment magnitudes are given as 8.4 and 8.5, respectively. The respective uniform slips are given as 9.3 and 11.3 m.

The region is sparsely populated, and only few population and economic centers exist among which are the four cities of Rabaul, Kokopo, Tarekukure, and Honiara (see Figure 4 for locations). Both scenarios produced $<$1 m tsunami amplitudes in Tarekukure and Honiara, but the simulated amplitudes reached ~10 m and ~2 m in Rabaul and Kokopo, respectively. Large amplification of tsunami amplitudes in Rabaul is due to the semienclosed shape of the gulf near Rabaul. For both hypothetical scenarios, Figures 4c and 4d showed that most of the tsunami energy was confined within the Solomon Sea and tsunami was not able to leave the area due to the presence of chain of islands and two submarine ridges in the south of the Solomon Sea. Similar propagation patterns were observed for the 29 March and 5 May 2015 tsunamis (Figures 4a and 4b); this is possibly the reason that these two tsunamis on 29 March and 5 May were not detectable in Honiara and were not recorded in other tide gauge stations in the region. Therefore, even large tsunami scenarios from New Britain subduction zone may not pose threats to far-field destinations such as Australia and New Zealand in the south.

The PNG earthquake doublet and hypothetical tsunamis studied in this article might help in advancing our worldwide understanding of earthquakes and tsunamis in several ways:

1. The rupture velocities were reliably estimated from joint use of seismic and tsunami data for the earthquake doublet, and they (i.e., 1.75 and 1.5 km/s) were smaller than V_r values previously assumed for tsunamigenic earthquakes.
2. Tsunamigenic earthquake doublets do not necessarily produce similar-size tsunamis; tsunami height is mostly controlled by the seafloor deformations generated by their parent earthquakes which can be different though the earthquake moment magnitudes are similar.
3. Ocean submarine ridges and island chains can significantly reflect back tsunami waves and limit the far-field reach of tsunamis.

5. Conclusions

We analyzed the 29 March and 5 May 2015 Kokopo, Papua New Guinea, earthquakes and tsunamis using teleseismic body wave inversion and tsunami simulation. Main findings are as follows:

1. Teleseismic body wave inversions using rupture velocities (V_r) ranging from 1.0 to 2.75 km/s with 0.25 km/s intervals showed almost similar results in terms of source-time functions and waveform agreements between the observed and simulated waveforms. The rupture durations were ~45 s and ~55 s for the March and May event, with their peaks at ~25 s and at ~17 s, respectively. However, the spatial distributions of the calculated slips were significantly different for assumed rupture velocities. We were unable to choose the best source model from the teleseismic body wave inversions for each earthquake.
2. Tsunami simulations using all slip distributions favored the one from $V_r = 1.75$ km/s for the March tsunami and $V_r = 1.5$ km/s for the May one in terms of arrival times, wave periods, and root-mean-square misfits of the tsunami waveforms. The largest slip on the fault was 2.1 m, and maximum seafloor uplift was ~ 0.4 m located ~35 km south of the epicenter for the March earthquake. The seismic moment of this source model was 2.15×10^{20} N m equivalent to the moment magnitude of 7.5. For the May event, the largest slip on the fault was 1.7 m but was located deeper. The seismic moment of this source model was 1.89×10^{20} N m equivalent to the moment magnitude of 7.45. The maximum seafloor deformation was ~ 0.2 m located ~15 km east of the epicenter.
3. The differences in the amounts and locations of maximum seafloor deformations yielded different tsunami sizes. This indicates that even though the earthquake size and rupture durations are similar for an earthquake doublet, the resultant tsunami would be different, depending on the location and depth of the earthquake source, as well as water depth around the source.
4. Simulations of two large tsunami scenarios from the New Britain subduction zone showed that the shoreline tide gauge zero-to-crest amplitude can reach up to 10 m in Rabaul. Most of the tsunami was confined within the Solomon Sea, indicating low tsunami hazards for far-field destinations such as Australia and New Zealand in the south. For other regions, ocean submarine ridges and island chains can significantly reflect back tsunami waves and limit the far-field reach of tsunamis.

Acknowledgments

The tide gauge records used in this study were provided by the Sea Level Station Monitoring Facility of Intergovernmental Oceanographic Commission (http://www.ioc-sealevelmonitoring.org/). Teleseismic waveforms were downloaded from the Incorporated Research Institutions for Seismology Data Management Center (IRIS DMC) website (http://www.iris.edu/wilber3/find_event). DART records of the tsunami were downloaded from the NOAA website at http://nctr.pmel.noaa.gov/Dart/. Most figures were drafted using the GMT software [*Wessel and Smith*, 1991]. We are sincerely grateful to Shingo Watada, Shigeki Nakagawa, Dun Wang, and Takeo Ishibe (all from ERI, University of Tokyo) for their detailed reviews of the manuscript before submission. This article benefited from constructive review comments from David R. Tappin (British Geological Survey, UK) for which we are sincerely grateful. This study was supported by the Japan Society for the Promotion of Science (JSPS).

The Editor thanks David Tappin for his assistance in evaluating this paper.

References

Bassin, C., G. Laske, and G. Masters (2000), The current limits of resolution for surface wave tomography in North America, *Eos Trans. AGU*, *81*, F897.

Chen, T., A. V. Newman, L. Feng, and H. M. Fritz (2009), Slip distribution from the 1 April 2007 Solomon Islands earthquake: A unique image of near-trench rupture, *Geophys. Res. Lett.*, *36*, L16307, doi:10.1029/2009GL039496.

Fritz, H. M., and N. Kalligeris (2008), Ancestral heritage saves tribes during 1 April 2007 Solomon Islands tsunami, *Geophys. Res. Lett. 35*, L01607, doi:10.1029/2007GL031654.

Geoware (2011), The Tsunami Travel Times (TTT). [Available at http://www.geoware-online.com/tsunami.html.]

Gusman, A. R., S. Murotani, K. Satake, M. Heidarzadeh, E. Gunawan, S. Watada, and B. Schurr (2015), Fault slip distribution of the 2014 Iquique, Chile, earthquake estimated from ocean-wide tsunami waveforms and GPS data, *Geophys. Res. Lett.*, *42*, 1053–1060, doi:10.1002/2014GL062604.

Heidarzadeh, M., and K. Satake (2015), Source properties of the 17 July 1998 Papua New Guinea tsunami based on tide gauge records, *Geophys. J. Int.*, *202*(1), 361–369.

Intergovernmental Oceanographic Commission, IHO and BODC (2003), Centenary edition of the GEBCO Digital Atlas, published on CD-ROM on behalf of the Intergovernmental Oceanographic Commission and the International Hydrographic Organization as part of the General Bathymetric Chart of the Oceans, British Oceanographic Data Centre, Liverpool, U. K.

Kennett, B. L. N., E. R. Engdahl, and R. Buland (1995), Constraints on seismic velocities in the Earth from travel times, *Geophys. J. Int.*, *122*, 108–124.

Kikuchi, M., and H. Kanamori (1991), Inversion of complex body waves–III, *Bull. Seismol. Soc. Am. 81*, 2335–2350.
Lay, T. (2012), Why giant earthquakes keep catching us out, *Nature*, *483*(7388), 149–150.
Lay, T., and H. Kanamori (1980), Earthquake doublets in the Solomon Islands, *Phys. Earth Planet. Int.*, *21*(4), 283–304.
Lay, T., H. Yue, E. E. Brodsky, and C. An (2014), The 1 April 2014 Iquique, Chile, M_w 8.1 earthquake rupture sequence, *Geophys. Res. Lett.*, *41*, 3818–3825, doi:10.1002/2014GL060238.
Mathworks (2015), *MATLAB User Manual*, 282 pp., The math Works Inc., Mass.
McAdoo, B. G., H. Fritz, K. L. Jackson, N. Kalligeris, J. Kruger, M. Bonte-Grapentin, A. L. Moore, W. B. Rafiau, D. Billy, and B. Tiano (2008), Solomon Islands tsunami, one year later, *Eos Trans. AGU*, *89*, 169–170.
McCaffrey, R. (2007), The next great earthquake, *Science*, *315*, 1675.
Murotani, S., K. Satake, and Y. Fujii (2013), Scaling relations of seismic moment, rupture area, average slip, and asperity size for $M \sim 9$ subduction-zone earthquakes, *Geophys. Res. Lett.*, *40*, 5070–5074, doi:10.1002/grl.50976.
Okada, Y. (1985), Surface deformation due to shear and tensile faults in a half-space, *Bull. Seismol. Soc. Am.*, *75*, 1135–1154.
Pegler, G., S. Das, and J. H. Woodhouse (1995), A seismological study of the eastern New Guinea and the western Solomon Sea regions and its tectonic implications, *Geophys. J. Int.*, *122*(3), 961–981.
Satake, K. (1987), Inversion of tsunami waveforms for the estimation of a fault heterogeneity: Method and numerical experiments, *J. Phys. Earth*, *35*(3), 241–254.
Satake, K. (1995), Linear and nonlinear computations of the 1992 Nicaragua earthquake tsunami, *Pure Appl. Geophys.*, *144*, 455–470.
Satake, K. (2014), Advances in earthquake and tsunami sciences and disaster risk reduction since the 2004 Indian Ocean tsunami, *Geosci. Lett.*, *1*, 1–13.
Satake, K., and B. F. Atwater (2007), Long-term perspectives on giant earthquakes and tsunamis at subduction zones, *Annu. Rev. Earth Planet. Sci.*, *35*, 349–374.
Stein, S., and E. A. Okal (2007), Ultralong period seismic study of the December 2004 Indian Ocean earthquake and implications for regional tectonics and the subduction process, *Bull. Seismol. Soc. Am.*, *97*, S279–S295.
Synolakis, C. E., J.-P. Bardet, J. C. Borrero, H. L. Davies, E. A. Okal, E. A. Silver, S. Sweet, and D. R. Tappin (2002), The slump origin of the 1998 Papua New Guinea tsunami, *Proc. R. Soc. Lond. A*, *458*, 763–789.
Tappin, D. R., P. Watts, G. M. McMurtry, Y. Lafoy, and T. Matsumoto (2001), The Sissano, Papua New Guinea tsunami of July 1998—Offshore evidence on the source mechanism, *Mar. Geol.*, *175*, 1–23.
United States Geological Survey (2015), United States Geological Survey, earthquake archives. [Available at http://earthquake.usgs.gov/earthquakes/search/.]
Wells, D. L., and K. J. Coppersmith (1994), New empirical relationships among magnitude, rupture length, rupture width, rupture area, and surface displacement, *Bull. Seismol. Soc. Am. 84*(4), 974–1002.
Wessel, P., and W. H. F. Smith (1991), Free software helps map and display data, *Eos Trans. AGU*, *72*, 441.
Yoneshima, S., K. Mochizuki, E. Araki, R. Hino, M. Shinohara, and K. Suyehiro (2005), Subduction of the Woodlark Basin at New Britain trench, Solomon Islands region, *Tectonophysics*, *397*(3), 225–239.